2016

Structural and Antiferromagnetic Properties of Ba(Fe1−x−yCoxRhy)2As2 compounds

M. G. Kim

T. W. Heitmann

Sean R. Mulcahy
Western Washington University, sean.mulcahy@wwu.edu

E. D. Bourret-Courchesne

R. J. Birgeneau

Recommended Citation
M. G. Kim, T. W. Heitmann, S. R. Mulcahy, E. D. Bourret-Courchesne, and R. J. Birgeneau Physical Review B 93, 094520 – Published 24 March 2016

Structural and antiferromagnetic properties of $Ba(Fe_{1-x-y}Co_xRh_y)_2As_2$ compounds

M. G. Kim,[1,*] T. W. Heitmann,[2] S. R. Mulcahy,[3,†] E. D. Bourret-Courchesne,[1] and R. J. Birgeneau[1,4,5]

[1]*Materials Sciences Division, Lawrence Berkeley National Laboratory, Berkeley, California 94720, USA*

[2]*The Missouri Research Reactor, University of Missouri, Columbia, Missouri 65211, USA*

[3]*Department of Earth and Planetary Science, University of California, Berkeley, California 94720, USA*

[4]*Department of Materials Science and Engineering, University of California, Berkeley, California 94720, USA*

[5]*Department of Physics, University of California, Berkeley, California 94720, USA*

(Received 9 December 2015; published 24 March 2016)

We present a systematic investigation of the electrical, structural, and antiferromagnetic properties for the series of $Ba(Fe_{1-x-y}Co_xRh_y)_2As_2$ compounds with fixed $x \approx 0.027$ and $0 \leqslant y \leqslant 0.035$. We compare our results for the Co-Rh doped $Ba(Fe_{1-x-y}Co_xRh_y)_2As_2$ compounds with the Co doped $Ba(Fe_{1-x}Co_x)_2As_2$ compounds. We demonstrate that the electrical, structural, antiferromagnetic, and superconducting properties of the Co-Rh doped compounds are similar to the properties of the Co doped compounds. We find that the overall behaviors of $Ba(Fe_{1-x-y}Co_xRh_y)_2As_2$ and $Ba(Fe_{1-x}Co_x)_2As_2$ compounds are very similar when the total number of extra electrons per Fe/TM (TM = transition metal) site is considered, which is consistent with the rigid band model. Despite the similarity, we find that the details of the transitions, for example, the temperature difference between the structural and antiferromagnetic transition temperatures and the incommensurability of the antiferromangetic peaks, are different between $Ba(Fe_{1-x-y}Co_xRh_y)_2As_2$ and $Ba(Fe_{1-x}Co_x)_2As_2$ compounds.

DOI: 10.1103/PhysRevB.93.094520

I. INTRODUCTION

The high-temperature superconductivity in the FeAs-based compounds is closely related to the underlying structural and magnetic properties. The parent $BaFe_2As_2$ compound exhibits structural and antiferromagnetic (AFM) phase transitions [1–5]. The structure changes from a tetragonal ($I4/mmm$) to an orthorhombic ($Fmmm$) structure [1–5]. The AFM transition occurs at a temperature (T_N) slightly lower than the structural transition temperature (T_S) and the AFM ordering is commensurate and characterized by the propagation vector $\boldsymbol{Q}_{AFM} = (1,0,1)$ in the orthorhombic notation [1–5].

Superconductivity in this system can be effectively achieved by tuning external parameters [3–5]. One of the parameters is doping by substituting transition-metal elements for Fe [3–12]. This is noted as electron or hole doping since these elements are considered to possess additional carriers when compared with Fe. With electron doping by transition-metal elements, particularly in $Ba(Fe_{1-x}TM_x)_2As_2$ with TM = Co [6,7], Ni [8,9], Rh [10,11], Pd [10,11], Ir [11], or Pt [12], the structural and AFM transitions are continuously suppressed to lower temperatures and the difference between T_S and T_N becomes larger with increasing substitution levels. Superconductivity emerges at a sufficient doping level, usually before the complete suppression of those transitions [3–12].

With the emergence of superconductivity, the superconducting and antiferromagnetic states compete for the same quasiparticles. As a result, when superconductivity becomes dominant, the AFM ordering is weakened, which is observed as the suppression of the AFM order parameter below the superconducting transition temperature (T_c) [13–17]. Since the crystal structure is coupled to the magnetism via the nematic order parameter [2,18], the structure of the system also alters below T_c. The orthorhombic structure becomes less orthorhombic below T_c and eventually reenters to a tetragonal phase at higher doping levels [18].

Detailed measurements of the AFM ordering by neutron diffraction also revealed that the commensurate (C) AFM order [19] becomes incommensurate (IC), $\boldsymbol{Q}_{AFM} + \boldsymbol{\tau}$ with a small incommensurability $\boldsymbol{\tau}$, at higher substitution levels in $Ba(Fe_{1-x}TM_x)_2As_2$ with TM = Co [20] and Ni [21]. Because the C and IC AFM phases coexist in certain doping levels, the C-to-IC transition is first order [20,21]. In contrast, nonsuperconducting electron doped $Ba(Fe_{1-x}Cu_x)_2As_2$ compounds do not show the C-to-IC transition while the suppression of the AFM ordering is similar to that in superconducting compounds [21]. Thus, not only the suppression of the AFM ordering but also the C-to-IC transition may be linked to the superconductivity in this system.

Intriguingly, a simple rigid band model can explain the properties of the electron doped superconducting compounds, $Ba(Fe_{1-x}TM_x)_2As_2$ [8,10,21]. In the rigid band picture, Co gives one electron more than Fe and Ni gives two electrons more than Fe; Ni doping affects the properties of the compound twice as effectively as Co doping [8,10,21]. When the phase diagrams of $Ba(Fe_{1-x}Co_x)_2As_2$ and $Ba(Fe_{1-x}Ni_x)_2As_2$ are plotted in terms of the number of extra electrons per the Fe/TM site, those phase diagrams lie on top of each other [8,10]. Similarly, the rigid band picture is also valid for Rh, Pd, and other electron doping elements that induce superconductivity. However, previous studies show that electron or hole doping in $Ba(Fe_{1-x}TM_x)_2As_2$ with TM = Cr [22], Mn [23,24], or Cu [8,21] show different magnetic properties and no superconductivity; this behavior deviates from the rigid band prediction.

It has been argued that aspects of the crystal structure, such as the pnictogen-Fe-pnictogen angle or the pnictogen height, may directly affect the superconducting properties [4,25,26]. From this point of view, one can imagine that the superconducting properties in $Ba(Fe_{1-x}Co_x)_2As_2$ and $Ba(Fe_{1-x}Rh_x)_2As_2$

*mgkim@lbl.gov

†Present address: Geology Department, Western Washington University, Bellingham, WA, 98225, USA; sean.mulcahy@wwu.edu

might be different due to the size difference between Co and Rh. While the size (disorder) effect on the structural and magnetic properties in these compounds needs a further study, the superconducting properties seem to be quite similar in $Ba(Fe_{1-x}Co_x)_2As_2$ and $Ba(Fe_{1-x}Rh_x)_2As_2$ [10]. Interestingly, as we discussed earlier, the structural, magnetic, and superconducting properties behave similarly in compounds in which the rigid band approximation seems valid, and one can imagine that the doping effect plays an important role in these compounds. Then, it is puzzling how the rigid band character would compete with the size (disorder) effect, how the physical properties are affected by disorder and doping at the same time.

Here, we present a systematic study of the electrical properties, lattice parameters, and structural and antiferromagnetic properties in $Ba(Fe_{1-x-y}Co_xRh_y)_2As_2$ compounds. We introduce simultaneous doping of Co and Rh in order to test the effect of doping and disorder. We find that the details of the crystal structures, observed by the lattice parameters a and c, are different in $Ba(Fe_{1-x}Co_x)_2As_2$, $Ba(Fe_{1-x}Rh_x)_2As_2$, and $Ba(Fe_{1-x-y}Co_xRh_y)_2As_2$ but the superconducting transition temperatures are similar in all these compounds. We show that the structural/AFM transitions, the AFM ordering, and their phase diagrams are quite similar in $Ba(Fe_{1-x-y}Co_xRh_y)_2As_2$, $Ba(Fe_{1-x}Co_x)_2As_2$, and $Ba(Fe_{1-x}Rh_x)_2As_2$, indicating that in the underdoped region, the rigid band picture is surprisingly successful in explaining the properties of Co and Rh doubly doped $Ba(Fe_{1-x-y}Co_xRh_y)_2As_2$ compounds.

II. EXPERIMENT

Single crystals of $Ba(Fe_{1-x-y}Co_xRh_y)_2As_2$ were grown out of a Fe/Co/Rh-As flux using conventional high-temperature flux growth. First, we prepared Fe/Co/Rh-As precursors with a ratio of Fe : Co : Rh : As $= (1-x-y) : x : y : 1$, which were sealed in an evacuated quartz tube. The prepared precursor powders were heated following the temperature steps described in Ref. [27]. Then the resulting precursor was mixed with Ba pieces in the ratio of Ba : $Fe_{1-x-y}Co_xRh_yAs = 1 : 4$, which was also sealed in an evacuated quartz tube. To grow single crystals, we applied the heating procedure described in Ref. [7] and we used the centrifugal decanting method at 1000 °C to separate crystals from the flux.

Compositional analyses were acquired using a Cameca SX-51 electron microprobe equipped with five tunable wavelength dispersive spectrometers (WDS). Analyses were conducted with a 20 keV accelerating voltage, 20 nA beam current, and 5 μm beam diameter. Peak and background count times for all elements were 10 s. Analyses yielded a relative uncertainty less than 5%. For our growth, we fixed the nominal (starting) Co concentration $x_{nom} = 0.032$ to achieve an actual target concentration of $x = 0.027$ while the nominal Rh concentrations were varied. From the WDS measurements, we find that the resulting (actual) Co concentrations vary between $x_{WDS} = 0.026$ and 0.029 and we do not find any correlations between the actual Co concentrations and the nominal Rh concentrations. Thus, we note $x \approx 0.027$ and show a summary of the nominal Rh concentration (y_{nom}) versus actual Rh concentration (y_{WDS}) in Fig. 1. This demonstrates that y_{WDS} increases roughly linearly with the nominal doping concentration for $Ba(Fe_{1-x-y}Co_xRh_y)_2As_2$ with $y_{WDS} \approx \frac{1}{2}y_{nom}$.

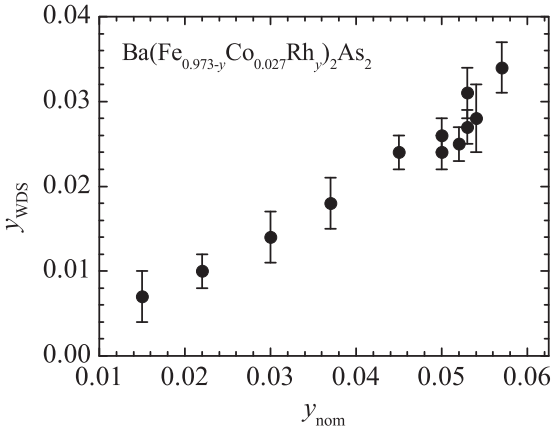

FIG. 1. Measured Rh concentration vs nominal Rh concentration for the $Ba(Fe_{1-x-y}Co_xRh_y)_2As_2$ with $x \approx 0.027$ compounds.

Electrical transport data were collected by a Quantum Design physical property measurement system (PPMS). Electrical contacts were made to the sample using Leitsilber 200 conductive silver paint to attach Au wires in a four-probe configuration. The measurements were done between $T = 2$ and 300 K. Powder x-ray diffraction data were collected at room temperature with a Siemens diffractometer using Cu $K\alpha_1$ radiation. Several small crystals from the same growth batch were collected and ground into powder for the measurements. The lattice parameters were obtained by the Le Bail extraction method using the RIETICA program [28].

For neutron diffraction measurements, single pieces of crystals with a typical mass of approximately 200 mg were selected from each growth batch. We performed the diffraction measurements at the TRIAX triple-axis spectrometer at the University of Missouri Research Reactor. The beam collimators before the monochromator, between the monochromator and sample, between the sample and analyzer, and between the analyzer and detector were 60′-40′-sample-40′-80′ collimation. We used fixed $E_i = E_f = 14.7$ meV and two pyrolytic graphite filters, one before the analyzer and one before the monochromator, to eliminate higher harmonics in the incident beam. Measurements were performed in a closed-cycle refrigerator between room temperature and the base temperature $T \approx 5$–7 K of the refrigerator. We define $\boldsymbol{Q} = (H,K,L) = \frac{2\pi}{a}H\hat{\imath} + \frac{2\pi}{b}K\hat{\jmath} + \frac{2\pi}{c}L\hat{k}$, where the orthorhombic lattice constants are $a \geqslant b \approx 5.6$ Å and $c \approx 13$ Å. Samples were studied in the vicinity of $\boldsymbol{Q}_{AFM} = (1,0,3)$ in the $(\zeta,K,3\zeta)$ plane, allowing a search for incommensurability along the $\boldsymbol{b}$ axis ($[0,K,0]$, transverse direction) as found for $Ba(Fe_{1-x}Co_x)_2As_2$ [20] and $Ba(Fe_{1-x}Ni_x)_2As_2$ [21]. All samples exhibited small mosaicities, $\leqslant 0.4°$ full width at half maximum (FWHM) measured by rocking scans, demonstrating high sample quality.

III. RESULTS AND DISCUSSION

We present normalized electrical resistance data between $T = 2$ and 300 K for selected $Ba(Fe_{1-x-y}Co_xRh_y)_2As_2$ compounds in Fig. 2. We measured as-grown samples to avoid shaping samples for the resistivity measurement to

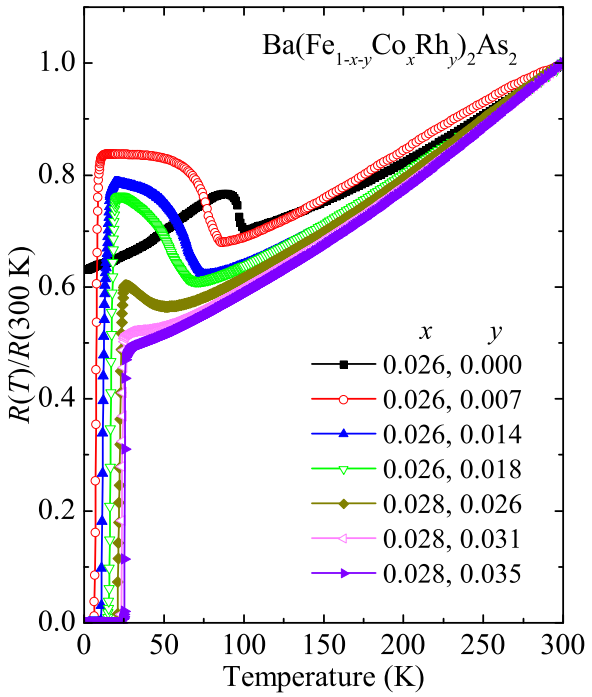

FIG. 2. The temperature-dependent resistance, normalized by the room temperature value, for $Ba(Fe_{1-x-y}Co_xRh_y)_2As_2$.

prevent cracks or exfoliation of the sample [7,8,10] and normalized our resistance data by the resistance value at $T = 300$ K for each measurement. We find anomalies in the resistance data, which represent T_S and T_N, as previously seen in transition-metal doped $BaFe_2As_2$ compounds [3–12]. For instance, the resistance anomalies appear at $T = 99.6$ K and $T = 96.5$ K for the sample with $x = 0.026$ and $y = 0.000$, which are consistent with the reported values of T_S and T_N for similar compositions, respectively [7,8]. These values are obtained from the derivative of the resistance data and an example of the derivative of the resistance data is shown in Fig. 3 for $Ba(Fe_{0.958}Co_{0.026}Rh_{0.016})_2As_2$. These anomalies appear at lower temperatures when more Rh is doped. In the

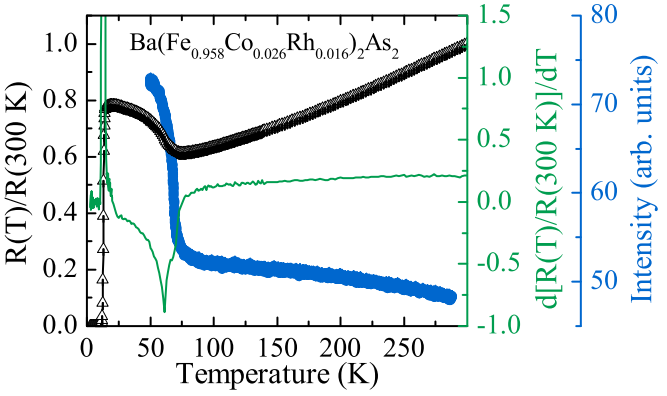

FIG. 3. Normalized resistance (open black triangles), the derivative of the resistance (green line), and the structural order parameter (closed blue circles) for $x + y = 0.042$, $Ba(Fe_{0.958}Co_{0.026}Rh_{0.016})_2As_2$.

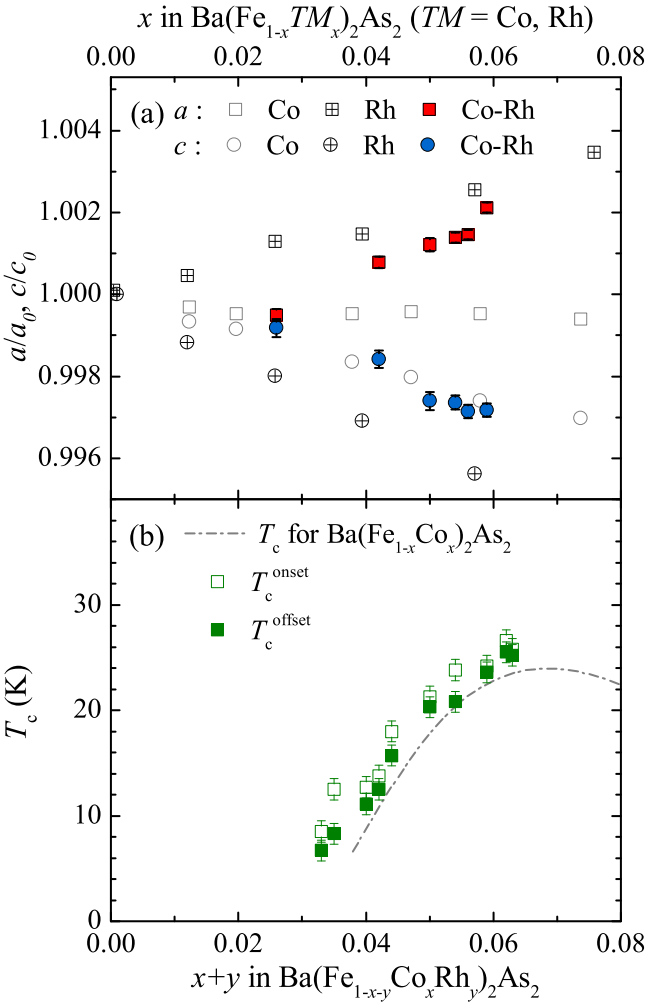

FIG. 4. (a) Normalized lattice parameters. Solid symbols show a/a_0 (square) and c/c_0 (circle) for $Ba(Fe_{1-x-y}Co_xRh_y)_2As_2$ as a function of the sum of x and y. $a_0 = 3.9697(1)$ Å and $c_0 = 13.0583(4)$ Å. Open and crossed symbols are a/a_0 and c/c_0 for $Ba(Fe_{1-x}Co_x)_2As_2$ and $Ba(Fe_{1-x}Rh_x)_2As_2$, respectively, from Ref. [10]. (b) Superconducting transition temperatures (T_c). Open symbols and solid symbols represent the onset and offset temperatures for $Ba(Fe_{1-x-y}Co_xRh_y)_2As_2$, respectively (see the text for details). The line indicates T_c for $Ba(Fe_{1-x}Co_x)_2As_2$ from Refs. [7,8].

sample with $x = 0.028$ and $y = 0.031$, we no longer see the resistance anomaly which indicates no structural and AFM transitions. Increasing the Rh concentration from $y = 0.000$ to 0.018 with a fixed actual Co concentration $x = 0.026$, and from $y = 0.026$ to 0.035 with $x = 0.028$ results in systematic decreases in T_S and T_N. This observation is consistent with the behaviors in $Ba(Fe_{1-x}Co_x)_2As_2$ and $Ba(Fe_{1-x}Rh_x)_2As_2$ [7,8]. Although it is not yet clear whether Co and Rh donate the same number of extra electrons per transition metal, we attempt to analyze and understand our data in terms of total electron doping and denote our data using the total doping $(x + y)$ in the rest of the paper, unless it is otherwise necessary.

Figure 4(a) shows the lattice parameters a and c at room temperature normalized by the values for the parent $BaFe_2As_2$ compound. For the sample with $x = 0.027$ and $y = 0.000$, i.e., $Ba(Fe_{0.973}Co_{0.027})_2As_2$, the normalized lattice parameters are

close to the previously reported values [7,8]. We find that the in-plane lattice parameter a increases whereas the out-of-plane lattice parameter c decreases with increasing Rh doping in $Ba(Fe_{0.973-y}Co_{0.027}Rh_y)_2As_2$. We compare our data with those for $Ba(Fe_{1-x}Co_x)_2As_2$ [7,8] and $Ba(Fe_{1-x}Rh_x)_2As_2$ [10], which are shown with open and crossed symbols, respectively, in Fig. 4(a). While a slight decrease is observed in the lattice parameter a for $Ba(Fe_{1-x}Co_x)_2As_2$, the lattice parameter a for $Ba(Fe_{1-x-y}Co_xRh_y)_2As_2$ increases significantly and follows the trend in $Ba(Fe_{1-x}Rh_x)_2As_2$. In contrast, the lattice parameter c for $Ba(Fe_{1-x-y}Co_xRh_y)_2As_2$ tracks closely the change in the lattice parameter c in $Ba(Fe_{1-x}Co_x)_2As_2$ whereas the lattice parameter c for $Ba(Fe_{1-x}Rh_x)_2As_2$ is much larger in all composition ranges.

Figure 4(b) presents the superconducting transition temperature (T_c) as a function of electron doping, $x + y$. The onset and offset T_c were determined from the resistance measurements using the criteria described in Ref. [29]. We find that the superconducting transition temperatures for $Ba(Fe_{1-x-y}Co_xRh_y)_2As_2$ [symbols in Fig. 4(b)] are very similar to those observed in $Ba(Fe_{1-x}Co_x)_2As_2$ and $Ba(Fe_{1-x}Rh_x)_2As_2$ [7,8]. For comparison, the T_c phase line for $Ba(Fe_{1-x}Co_x)_2As_2$ is shown as the dotted-dashed line in Fig. 4(b). Earlier studies have argued that the details of the crystal structure, such as the pnictogen-Fe-pnictogen angle and the pnictogen height, may play a significant role in high T_c [4,25,26]. Although we do not precisely know these details, we can deduce that such details are likely different between $Ba(Fe_{1-x}Co_x)_2As_2$, $Ba(Fe_{1-x}Rh_x)_2As_2$, and $Ba(Fe_{1-x-y}Co_xRh_y)_2As_2$ based on the behaviors of the lattice parameters a and c in these compounds. Despite this potential difference, superconductivity is surprisingly robust in $Ba(Fe_{1-x}Co_x)_2As_2$, $Ba(Fe_{1-x}Rh_x)_2As_2$, and $Ba(Fe_{1-x-y}Co_xRh_y)_2As_2$, as shown in Fig. 4(b).

Now we turn to the results of the single-crystal neutron diffraction measurements. We first present the structural order parameters in Fig. 5 which were obtained by measuring changes of the peak intensity at the nuclear (4,0,0) peak as a function of temperature. The change in the peak intensity is associated with an extinction release across a structural phase transition [13,30,31]. Measurements of extinction release as a surrogate structural order parameter are very sensitive to the quality of the samples and usually result in various shapes of order parameters (see the figures in Refs. [13,30–32]) which make the determination of T_S difficult. So we first determined T_S from the order parameters at a temperature where the intensity increases sharply. Then we compared this T_S with the temperature where the resistivity anomaly is observed. An example of this method is shown in the Fig. 3 for $Ba(Fe_{0.958}Co_{0.026}Rh_{0.016})_2As_2$. Since the values from two different measurements are consistent with each other, we can rely on this method to determine T_S. In Fig. 5, the T_S is obtained from this method and marked with arrows.

Figures 5(a)–5(c) show the effect of Rh doping on the structural transition in $Ba(Fe_{1-x-y}Co_xRh_y)_2As_2$. In Fig. 5(a), the structural transition occurs at $T_S = 69 \pm 1$ K in the $x = 0.026$ and $y = 0.016$ compound and it is reduced to $T_S = 48 \pm 1$ K in the $x = 0.026$ and $y = 0.024$. T_S is reduced by approximately 20 K with $\Delta y = 0.008$ and a fixed $x = 0.026$. With slightly more Co and Rh doping [Figs. 5(b) and 5(c)], $Ba(Fe_{1-x-y}Co_xRh_y)_2As_2$ compounds become superconducting (Fig. 2) and show that the intensity at (4,0,0) decreases below T_c [Figs. 5(b)–5(d)]; as the crystal structure becomes less orthorhombic, a part of the diffracted intensity becomes extinct. This is consistent with the suppression of the structural order parameter which is commonly observed in superconducting $Ba(Fe_{1-x}Co_x)_2As_2$ and $Ba(Fe_{1-x}Rh_x)_2As_2$ compounds [13,18]. In Fig. 5(b), $T_S = 43 \pm 1$ K in the $x = 0.028$ and $y = 0.026$ compound and it is decreased to 30 ± 1 K in the $x = 0.028$ and $y = 0.031$ compound. T_S is suppressed by 13 K with $\Delta y = 0.005$ and a fixed $x = 0.028$. The decrease in T_S in Fig. 5(c) becomes much smaller (≈ 2 K) with a smaller $\Delta y = 0.001$ and a fixed $x = 0.029$. $T_S = 41 \pm 1$ K for $y = 0.027$ and $T_S = 39 \pm 1$ K for $y = 0.028$. This trend in T_S with increasing Rh doping with fixed x values is consistent with the trend observed in electron doped $Ba(Fe_{1-x}Co_x)_2As_2$. Thus, we present the data with the total doping ($x + y$). Figure 5(d) shows a systematic suppression of the structural transition temperature as the total electron doping increases from $x + y = 0.042$ to 0.059. The structural transition disappears abruptly at $x + y = 0.060$. It is worth noting that for the $x + y = 0.059$ sample, the peak intensities below $T \approx 17$ K are almost the same as the value at T_S. This

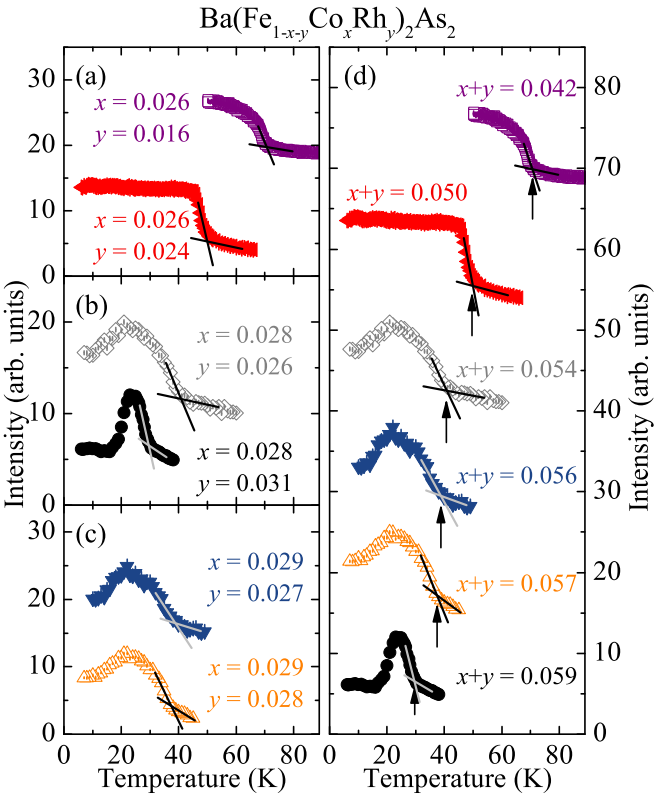

FIG. 5. Changes of the peak intensity at the nuclear (4,0,0) Bragg peak as a function of temperature for (a) $y = 0.016$ and 0.024 with a fixed $x = 0.026$, (b) $y = 0.026$ and 0.031 with a fixed $x = 0.028$, (c) $y = 0.027$ and 0.028 with a fixed $x = 0.029$, and (d) as a function of total doping ($x + y$). The structural transition temperature (T_S, the position of arrows) was determined at the point where the peak intensity raises sharply and the resistivity anomaly appears. Note the decrease of the subsequent peak intensity below T_c in $x + y \geqslant 0.054$. The data are arbitrarily offset vertically for clarity.

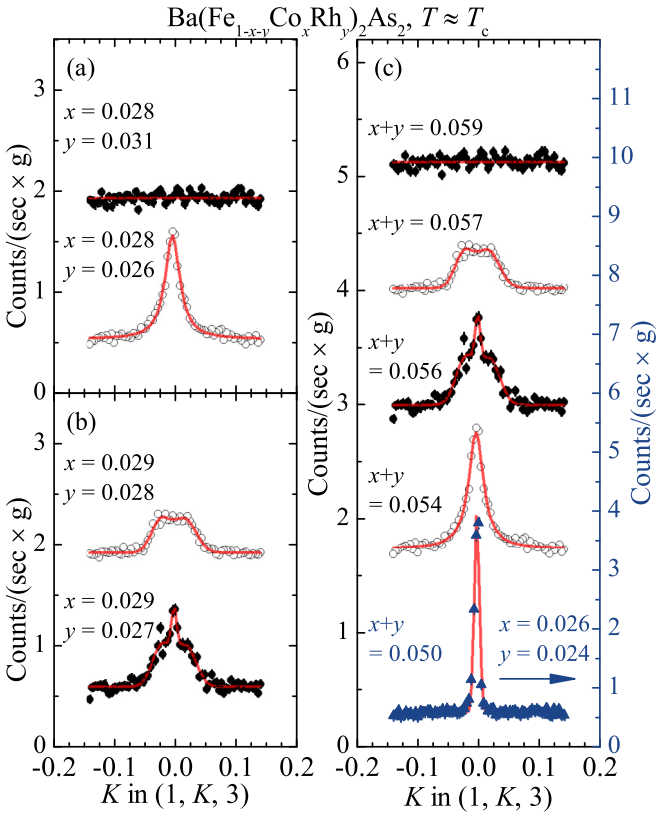

FIG. 6. Transverse neutron scattering near the (1,0,3) magnetic Bragg point at $T \approx T_c$ for (a) $y = 0.026$ and 0.031 with a fixed $x = 0.028$ and (b) $y = 0.027$ and 0.028 with a fixed $x = 0.029$. The same set of scans are shown in (c) as a function of $x + y$. Scans are normalized to counts/sec × g and are offset vertically for clarity. Data points far away from $K = 0$ serve the background that are identical in all scans.

implies that this sample reenters a tetragonal structure below $T \approx 17$ K. We conclude that the structure of $x + y = 0.059$ changes first from tetragonal to orthorhombic at $T_S = 30$ K and reenters a tetragonal structure at $T \approx 17$ K which is below T_c.

Figure 6 presents scans along the transverse direction, i.e., the orthorhombic $\boldsymbol{b}$ direction, through the (1,0,3) AFM Bragg position in $Ba(Fe_{1-x-y}Co_xRh_y)_2As_2$. We plot the scans at $T \approx T_c$ where the AFM signal is maximum. We first compare scans for compounds with the same amount of Co doping. Figure 6(a) shows scans for $y = 0.026$ and 0.031 with a fixed $x = 0.028$. While a single Lorentzian peak was observed for $y = 0.026$ ($x = 0.028$), no signals were observed for $y = 0.031$ ($x = 0.028$), showing that the AFM ordering is completely suppressed by increasing Rh doping ($\Delta y = 0.005$) with $x = 0.028$. Figure 6(b) shows scans for $y = 0.027$ and 0.028 with a fixed $x = 0.029$. We observed three peaks that consist of one central commensurate (C) peak at $\boldsymbol{Q}_{AFM}$ and two satellite incommensurate (IC) peaks at $\boldsymbol{Q}_{AFM} \pm \boldsymbol{\tau}$ for $y = 0.027$ ($x = 0.029$). Observation of three peaks indicates the coexistence of C and IC AFM phases in this sample, which is consistent with a first-order C-to-IC transition [20,21]. With a slight increase of Rh doping by $\Delta y = 0.001$, only IC AFM peaks remain at $T \approx T_c$ for $y = 0.028$ with $x = 0.029$. Although the Co concentrations were not the same for scans in Figs. 6(a) and 6(b), the effect of Rh doping is dominant in the AFM ordering in the studied compounds. Thus, we summarize this result in Fig. 6(c) with the total doping ($x + y$). A sharp single AFM peak is observed for $x + y \leqslant 0.050$, which is consistent with the commensurate (C) AFM ordering. With slightly more electron doping, the peak becomes broad along the orthorhombic $\boldsymbol{b}$ direction in $x + y = 0.054$, similar to the observation in other electron doped compounds [21]. Then, three peaks are observed at $x + y = 0.056$. With further Rh doping, only IC AFM peaks remain at $T \approx T_c$ for $x + y = 0.057$. Finally, we no longer detect any signals around $\boldsymbol{Q}_{AFM}$ for $x + y = 0.059$ and conclude that the AFM ordering is completely suppressed in samples with $x + y \geqslant 0.059$. The smooth evolution of the AFM ordering and the first-order C-to-IC transition are consistent with the behavior seen in superconducting Co or Ni doped compounds [20,21]. In addition, the critical concentration $x + y = 0.056$ of a first-order C-to-IC transition in $Ba(Fe_{1-x-y}Co_xRh_y)_2As_2$ is the same as the value ($x_c = 0.056$) observed for $Ba(Fe_{1-x}Co_x)_2As_2$ [20]. We fit the scans with a single Gaussian peak for $x + y = 0.050$, a single Lorentzian for $x + y = 0.054$, three Gaussian peaks for $x + y = 0.056$, and two Gaussian peaks for $x + y = 0.057$, and show the results of the best fits with lines in Fig. 6. From the fits for $x + y = 0.056$ and 0.057, we find that the incommensurability τ for both compounds is 0.020 ± 0.002 reciprocal lattice units (r.l.u.), which are identical within the error. This value is slightly smaller than the values for the single Co ($\tau \approx 0.025$–0.030) or Ni ($\tau = 0.033$) doped compounds [20,21].

In order to study the temperature dependence of the AFM ordering, we plot transverse scans at three different temperature regimes and the corresponding order parameters in Fig. 7. For $x + y = 0.042$ and 0.050, a single sharp AFM peak exists down to the lowest temperature [Figs. 7(a) and 7(b)]. While the AFM peak for $x + y = 0.042$ increases continuously [Fig. 7(e)], the intensity of the peak for $x + y = 0.050$ increases first then decreases below T_c [Fig. 7(f)]. For $x + y = 0.056$, three AFM peaks are observed at all temperatures below T_N [Fig. 7(c)]. As temperature is lowered through T_c, the order parameter measured at the C AFM position is suppressed [Fig. 7(g)]. When we compare the scans between $T \approx T_c$ [solid red circles in Fig. 7(c)] and $T < T_c$ [open blue circles in Fig. 7(c)], we find that the intensities of the C and IC peaks decrease at a similar rate below T_c. For the compound with $x + y = 0.057$, we observed only two IC AFM peaks at $T \approx T_c$ (Fig. 6). At $T < T_c$, the order parameter measured at the C AFM position is suppressed, as expected from the competition between magnetism and superconductivity [Fig. 7(h)]. However, we observe three AFM peaks at $T < T_c$ in the compound with $x + y = 0.057$. It is likely that the central C AFM peak is present but not distinguishable at $T \approx T_c$ [Fig. 7(d)]. By looking at the intensity changes across T_c between the central C peak and the satellite IC peaks, we find that the suppression of the IC peaks is greater than that of the C AFM peak. This observation suggests that the C AFM may be more stable than the IC AFM in the competition with superconductivity. It is interesting to note that the nonsuperconducting Cu doped $Ba(Fe_{1-x}Cu_x)_2As_2$ compounds exhibit commensurate AFM ordering in the entire composition range. Since we only

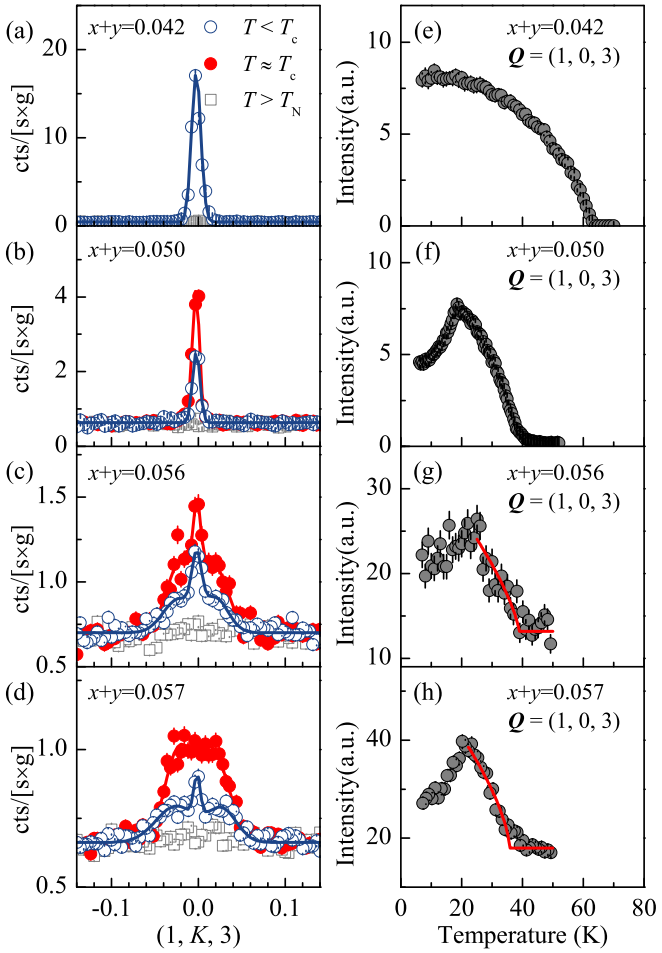

FIG. 7. Transverse neutron diffraction scans through the (1,0,3) magnetic Bragg peak at temperature $T < T_c$ (open blue circles), $T \approx T_c$ (solid red circles), and $T > T_N$ (open gray rectangles) for $Ba(Fe_{1-x-y}Co_xRh_y)_2As_2$ with (a) $x + y = 0.042$, (b) 0.050, (c) 0.056, and (d) 0.057. The corresponding AFM order parameters are shown in (e)–(h). Lines are guides to the eyes.

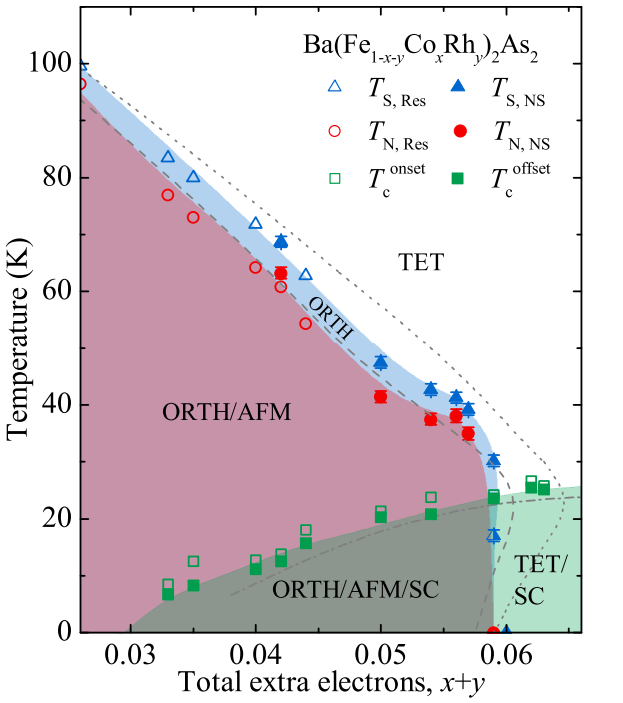

FIG. 8. Experimental phase diagram for $Ba(Fe_{1-x-y}Co_xRh_y)_2As_2$ determined from neutron diffraction (solid triangles and circles) and transport measurements (open triangles, circles, rectangles, and soid rectangles) as well as the data from the single Co doping (gray lines) [7,8,17,18]. Tetragonal (Tet), orthorhombic (Orth), antiferromangetic (AFM), and superconducting (SC) phases are noted and color coded. The reentrance temperature from the orthorhombic to tetragonal phase for $x + y = 0.059$ is denoted with a half-solid triangle.

have detailed Q scans at three temperatures, as presented here, and the AFM order parameters were measured at the Q_{AFM} position, further studies are required to understand this behavior and a possible connection to the superconductivity.

IV. SUMMARY

We summarize our results in the phase diagram of $Ba(Fe_{1-x-y}Co_xRh_y)_2As_2$ compounds in Fig. 8. The phase diagram is constructed from the transport and neutron measurements together with the phase lines of $Ba(Fe_{1-x}Co_x)_2As_2$. We see that while the AFM phase transition temperatures in $Ba(Fe_{1-x-y}Co_xRh_y)_2As_2$ are comparable to the values for $Ba(Fe_{1-x}Co_x)_2As_2$, the structural transition temperatures are lower for $Ba(Fe_{1-x-y}Co_xRh_y)_2As_2$. Consequently, the difference between T_S and T_N is smaller for $Ba(Fe_{1-x-y}Co_xRh_y)_2As_2$. At a higher doping level, both the structural and AFM phase transitions terminate at about $x + y = 0.059$ in $Ba(Fe_{1-x-y}Co_xRh_y)_2As_2$, which is smaller than $x \approx 0.06$ and 0.064 (for AFM and structural phase transitions, respectively) for $Ba(Fe_{1-x}Co_x)_2As_2$. However, the critical concentration for the C-to-IC AFM transition is similar in $Ba(Fe_{1-x-y}Co_xRh_y)_2As_2$ and $Ba(Fe_{1-x}Co_x)_2As_2$. The backbending of both the structural and AFM phase lines, observed in $Ba(Fe_{1-x}Co_x)_2As_2$ (dotted and dashed lines, respectively, in Fig. 8), are not clearly present in $Ba(Fe_{1-x-y}Co_xRh_y)_2As_2$. In addition the backbending was not observed for the Ni doped compounds. Instead, the phase lines for the Ni doped compounds disappeared very suddenly, resulting in an avoided quantum critical point [33], which may be the case for $Ba(Fe_{1-x-y}Co_xRh_y)_2As_2$. We observed surprising agreement between the superconducting transition temperatures in $Ba(Fe_{1-x-y}Co_xRh_y)_2As_2$ and $Ba(Fe_{1-x}Co_x)_2As_2$ while the details of structure, seen from systematic measurements of the lattice parameters, are different in the two compounds. This indicates that the electron doping plays the essential role in determining the T_c in this family of FeAs-based compounds.

Taken together, we have shown that the changes in the structural and antiferromagnetic phase transitions, suppression of their order parameters below T_c, and the emergence of superconductivity in $Ba(Fe_{1-x-y}Co_xRh_y)_2As_2$ compounds are very similar to those in $Ba(Fe_{1-x}Co_x)_2As_2$ compounds, whereas the fine details of those properties are slightly different between both materials. This clearly indicates that a simple rigid band picture works well in explaining the overall properties of electron doped superconducting $BaFe_2As_2$ compounds including $Ba(Fe_{1-x-y}Co_xRh_y)_2As_2$ compounds.

ACKNOWLEDGMENTS

We are grateful to M. Wang and Z. Xu for valuable discussions. The work at the Lawrence Berkeley National Laboratory was supported by the U.S. Department of Energy (DOE), Office of Basic Energy Sciences, Materials Sciences and Engineering Division, under Contract No. DE-AC02-05CH11231.

[1] Q. Huang, Y. Qiu, W. Bao, M. A. Green, J. W. Lynn, Y. C. Gasparovic, T. Wu, G. Wu, and X. H. Chen, Phys. Rev. Lett. **101**, 257003 (2008).

[2] M. G. Kim, R. M. Fernandes, A. Kreyssig, J. W. Kim, A. Thaler, S. L. Bud'ko, P. C. Canfield, R. J. McQueeney, J. Schmalian, and A. I. Goldman, Phys. Rev. B **83**, 134522 (2011).

[3] P. C. Canfield and S. L. Bud'ko, Annu. Rev. Condens. Matter Phys. **1**, 27 (2010).

[4] D. Johnston, Adv. Phys. **59**, 803 (2010).

[5] P. Dai, Rev. Mod. Phys. **87**, 855 (2015).

[6] A. S. Sefat, R. Jin, M. A. McGuire, B. C. Sales, D. J. Singh, and D. Mandrus, Phys. Rev. Lett. **101**, 117004 (2008).

[7] N. Ni, M. E. Tillman, J.-Q. Yan, A. Kracher, S. T. Hannahs, S. L. Bud'ko, and P. C. Canfield, Phys. Rev. B **78**, 214515 (2008).

[8] P. C. Canfield, S. L. Bud'ko, N. Ni, J. Q. Yan, and A. Kracher, Phys. Rev. B **80**, 060501 (2009).

[9] L. J. Li, Y. K. Luo, Q. B. Wang, H. Chen, Z. Ren, Q. Tao, Y. K. Li, X. Lin, M. He, Z. W. Zhu, G. H. Cao, and Z. A. Xu, New J. Phys. **11**, 025008 (2009).

[10] N. Ni, A. Thaler, A. Kracher, J. Q. Yan, S. L. Bud'ko, and P. C. Canfield, Phys. Rev. B **80**, 024511 (2009).

[11] F. Han, X. Zhu, P. Cheng, G. Mu, Y. Jia, L. Fang, Y. Wang, H. Luo, B. Zeng, B. Shen, L. Shan, C. Ren, and H. H. Wen, Phys. Rev. B **80**, 024506 (2009).

[12] S. R. Saha, T. Drye, K. Kirshenbaum, N. P. Butch, P. Y. Zavalij, and J. Paglione, J. Phys.: Condens. Matter **22**, 072204 (2010).

[13] A. Kreyssig, M. G. Kim, S. Nandi, D. K. Pratt, W. Tian, J. L. Zarestky, N. Ni, A. Thaler, S. L. Bud'ko, P. C. Canfield, R. J. McQueeney, and A. I. Goldman, Phys. Rev. B **81**, 134512 (2010).

[14] M. Wang, H. Luo, J. Zhao, C. Zhang, M. Wang, K. Marty, S. Chi, J. W. Lynn, A. Schneidewind, S. Li, and P. Dai, Phys. Rev. B **81**, 174524 (2010).

[15] D. K. Pratt, W. Tian, A. Kreyssig, J. L. Zarestky, S. Nandi, N. Ni, S. L. Bud'ko, P. C. Canfield, A. I. Goldman, and R. J. McQueeney, Phys. Rev. Lett. **103**, 087001 (2009).

[16] A. D. Christianson, M. D. Lumsden, S. E. Nagler, G. J. MacDougall, M. A. McGuire, A. S. Sefat, R. Jin, B. C. Sales, and D. Mandrus, Phys. Rev. Lett. **103**, 087002 (2009).

[17] R. M. Fernandes, D. K. Pratt, W. Tian, J. Zarestky, A. Kreyssig, S. Nandi, M. G. Kim, A. Thaler, N. Ni, P. C. Canfield, R. J. McQueeney, J. Schmalian, and A. I. Goldman, Phys. Rev. B **81**, 140501 (2010).

[18] S. Nandi, M. G. Kim, A. Kreyssig, R. M. Fernandes, D. K. Pratt, A. Thaler, N. Ni, S. L. Bud'ko, P. C. Canfield, J. Schmalian, R. J. McQueeney, and A. I. Goldman, Phys. Rev. Lett. **104**, 057006 (2010).

[19] M. G. Kim, A. Kreyssig, Y. B. Lee, J. W. Kim, D. K. Pratt, A. Thaler, S. L. Bud'ko, P. C. Canfield, B. N. Harmon, R. J. McQueeney, and A. I. Goldman, Phys. Rev. B **82**, 180412 (2010).

[20] D. K. Pratt, M. G. Kim, A. Kreyssig, Y. B. Lee, G. S. Tucker, A. Thaler, W. Tian, J. L. Zarestky, S. L. Bud'ko, P. C. Canfield, B. N. Harmon, A. I. Goldman, and R. J. McQueeney, Phys. Rev. Lett. **106**, 257001 (2011).

[21] M. G. Kim, J. Lamsal, T. W. Heitmann, G. S. Tucker, D. K. Pratt, S. N. Khan, Y. B. Lee, A. Alam, A. Thaler, N. Ni, S. Ran, S. L. Bud'ko, K. J. Marty, M. D. Lumsden, P. C. Canfield, B. N. Harmon, D. D. Johnson, A. Kreyssig, R. J. McQueeney, and A. I. Goldman, Phys. Rev. Lett. **109**, 167003 (2012).

[22] K. Marty, A. D. Christianson, C. H. Wang, M. Matsuda, H. Cao, L. H. VanBebber, J. L. Zarestky, D. J. Singh, A. S. Sefat, and M. D. Lumsden, Phys. Rev. B **83**, 060509 (2011).

[23] M. G. Kim, D. K. Pratt, G. E. Rustan, W. Tian, J. L. Zarestky, A. Thaler, S. L. Bud'ko, P. C. Canfield, R. J. McQueeney, A. Kreyssig, and A. I. Goldman, Phys. Rev. B **83**, 054514 (2011).

[24] A. Thaler, H. Hodovanets, M. S. Torikachvili, S. Ran, A. Kracher, W. Straszheim, J. Q. Yan, E. Mun, and P. C. Canfield, Phys. Rev. B **84**, 144528 (2011).

[25] K. Kuroki, H. Usui, S. Onari, R. Arita, and H. Aoki, Phys. Rev. B **79**, 224511 (2009).

[26] M. J. Calderon, B. Valenzuela, and E. Bascones, New J. Phys. **11**, 013051 (2009).

[27] Y. Chen, X. Lu, M. Wang, H. Luo, and S. Li, Supercond. Sci. Technol. **24**, 065004 (2011).

[28] RIETICA program available at www.rietica.org/index.htm.

[29] N. Ni, S. L. Bud'ko, A. Kreyssig, S. Nandi, G. E. Rustan, A. I. Goldman, S. Gupta, J. D. Corbett, A. Kracher, and P. C. Canfield, Phys. Rev. B **78**, 014507 (2008).

[30] C. Lester, J.-H. Chu, J. G. Analytis, S. C. Capelli, A. S. Erickson, C. L. Condron, M. F. Toney, I. R. Fisher, and S. M. Hayden, Phys. Rev. B **79**, 144523 (2009).

[31] X. Lu, J. T. Park, R. Zhang, H. Luo, A. H. Nevidomskyy, Q. Si, and P. Dai, Science **345**, 657 (2014).

[32] M. G. Kim, M. Wang, G. S. Tucker, P. N. Valdivia, D. L. Abernathy, S. Chi, A. D. Christianson, A. A. Aczel, T. Hong, T. W. Heitmann, S. Ran, P. C. Canfield, E. D. Bourret-Courchesne, A. Kreyssig, D. H. Lee, A. I. Goldman, R. J. McQueeney, and R. J. Birgeneau, Phys. Rev. B **92**, 214404 (2015).

[33] X. Lu, H. Gretarsson, R. Zhang, X. Liu, H. Luo, W. Tian, M. Laver, Z. Yamani, Y.-J. Kim, A. H. Nevidomskyy, Q. Si, and P. Dai, Phys. Rev. Lett. **110**, 257001 (2013).